Elastic thickness structure of South America estimated using wavelets and satellite-derived gravity data

Andrés Tassara [a,*], Chris Swain [b], Ron Hackney [c], Jon Kirby [b]

[a] *Institut für Geologische Wissenschaften, Freie Universität Berlin, Malteserstrasse, 74-100, D-12249 Berlin, Germany*
[b] *Western Australian Centre for Geodesy, Curtin University of Technology, GPO, Box U1987, Perth 6845, Australia*
[c] *Institut für Geowissenshaften, Christian-Albrechts-Universität zu Kiel, Otto-Hahn-Platz 1, D-24118 Kiel, Germany*

Abstract

We used a wavelet formulation of the classical spectral isostatic analysis to invert satellite-derived gravity and topography/bathymetry for elastic thickness (T_e) over South America and its surrounding plates. To provide a homogeneous representation of the gravity field for this vast region, we corrected free-air anomalies derived from a combination of terrestrial/marine gravity data with data from the GRACE and CHAMP satellite missions (model EIGEN-CG03C) by a simple Bouguer slab using a smoothed representation of surface relief (wavelengths > 125 km). The resulting Bouguer anomaly compares well with terrestrial data acquired in the Central Andes and allows T_e to be confidently estimated for values greater than 10 km. The T_e map resolves regional-scale features that are well-correlated with known surface structures and shows maximum values of 100 ± 15 km over the Archean–Neoproterozoic core of the continent, decreasing to less than 30 km around continental margins. Several regions of the oceanic plates and continental margins have an elastic thickness less than 10 km. We performed a quantitative analysis by comparing the elastic thickness with the thermal structure predicted from the age of oceanic crust and igneous–metamorphic rocks. This demonstrates that oceanic plates have been weakened by thermal interaction with hotspots and locally by fracturing and hydration near the trench. We observe that only the nucleus of the continent has resisted the thermomechanical weakening induced by the rifting of Africa and South America along the passive margin and the Andean orogeny along the active margin. This latter region shows along-strike variations in T_e that correlate with the geotectonic segmentation of the margin and with the pattern of crustal seismicity. Our results reveal that the rigidity structure follows the segmentation of the seismogenic zone along the subduction fault, suggesting a causal relationship that should be investigated in order to improve the understanding and predictability of great earthquakes and tsunamis.
© 2006 Elsevier B.V. All rights reserved.

* Corresponding author. Present address: Departamento de Geofisica, Facultad de Ciencias Físicas y Matemáticas, Universidad de Chile, Blanco Encalada 2002, Santiago, Chile. Tel.: +56 2 9784568; fax: +56 2 6968686.
E-mail addresses: andres@dgf.uchile.cl (A. Tassara), c_swain@wt.com.au (C. Swain), rhackney@geophysik.uni-kiel.de (R. Hackney), j.kirby@curtin.edu.au (J. Kirby).

1. Introduction

Mechanical strength is a fundamental property of the continental lithosphere that controls its response to long-term forces and, therefore, the temporal evolution and spatial configuration of continents. It can be parameterised

through the flexural rigidity $D \equiv E\,T_e^3/12(1-v^2)$ [1,2], which is a measure of the resistance of the lithosphere to flexure in response to loading. Young's modulus, E, and Poisson's ratio, v are material properties commonly treated as constant (10^{11} Pa and 0.25 in this work). With this assumption, D depends entirely on the elastic thickness T_e. This parameter can be defined as the thickness of an 'imaginary' elastic plate overlying an inviscid substratum [3] that would bend by the same amount as the 'real' lithosphere under the same applied loads [4]. Comparing values of T_e estimated from thin elastic plate rheology and surface observables (e.g. direct observations of deflection, gravity anomalies, seismic images) against more realistic rheological models (brittle–elastic–ductile) has proved to be a powerful tool for constraining the role played by different factors (e.g. compositional structure, geothermal gradient, tectonic forces) that influence lithospheric dynamics [3–10].

A number of different methods can be used to estimate values of T_e from surface observables (see a review in Watts [1] and the new methods proposed by Mantovani et al. [11], Braitenberg et al. [12], Simons et al. [13], Stark et al. [14], Kirby and Swain [15] and Jordan and Watts [16]). Forsyth [17] formulated an inversion technique that involves fitting the observed coherence and admittance between gravity and topography in the spectral domain to the predictions of a model where a thin elastic plate is flexed by surface and subsurface loads. Although there is some debate about the significance of T_e estimated by these means [18,19], most authors validate and extend Forsyth's method using different spectral estimators that are based on the Fast Fourier Transform (FFT), and covering the studied regions with data windows from which one T_e value is recovered [4,6,20–23]. However, it is well known that the size of the analysing window can significantly bias the estimated T_e [4,20]. To overcome this problem, some authors [13–15] have recently proposed the use of the continuous wavelet transform (CWT) for spectral isostatic analysis. The advantage of this method is that through the CWT, one can analyse the local spectrum of a two-dimensional (2D) signal for a given point in the spatial domain, owing to the ability of this transform to zoom in and out in the wavenumber domain by dilating a so-called mother wavelet function. Thus, the spectrum of the signal can be obtained for each node of a data grid, making possible the application of Forsyth's method with high spatial resolution and without the biases inherent to the classical FFT-based methods.

In this manuscript, we use the CWT-based method being developed by two of us [15,24–26] to compute a high-resolution map of elastic thickness for the South American continent and its surroundings. This continent has a rich geotectonic diversity and, therefore, it is ideally suited to studies of the relationship between the strength of the continental lithosphere, the thermal age of different tectonic provinces, their geological structure and active tectomagmatic processes. To do this work, we first computed a Bouguer anomaly grid from the global gravity model EIGEN-CG03C that combines terrestrial/marine gravity data with results of the CHAMP and GRACE satellite missions [27]. To the best of our knowledge, this is the first time that such a global model is used for the computation of Bouguer anomalies in order to estimate the elastic thickness. We validate the use of these data by observing that the derived Bouguer anomaly compares well with terrestrial gravity data for the Central Andes region, and that both databases give similar estimates of T_e. In the discussion, we compare our map with previously published T_e estimates for western South America and advance an interpretation of some significant features evident in our results. This interpretation demonstrates that the method we used efficiently recovers the expected spatial variations of lithospheric strength between different tectonic provinces and reveals new insights into the nature of the South American lithosphere.

2. South America and surrounding plates

The geotectonic setting of the South America plate and its surroundings is summarized in Fig. 1.

The South American continent is a mosaic of morphotectonic provinces spanning a wide range of geological features. The eastern, old core of the continent is formed by a series of Archaean to Palaeoproterozoic cratons (Amazonia, Sao Fransisco, Rio de la Plata) that are separated from each other by Meso- to Neoproterozoic mobile belts [30,31]. The Transbrasiliano Lineament is an old lithospheric structure associated with one of these belts but, significantly, it concentrates active seismicity [33]. During the Phanerozoic, some of the regions between the Precambrian fragments became the centre of intracontinental basins (Amazon and Paraná). These basins were also the focus of Mesozoic flood basalt volcanism contemporaneous with the rifting between South America and Africa and the opening of the Atlantic ocean [34–36]. This process started at 130 Ma in the south and propagated northward until 90 Ma, as revealed by the age of the oceanic part of the South America plate along the eastern, passive margin of the continent [32] (see Fig. 1).

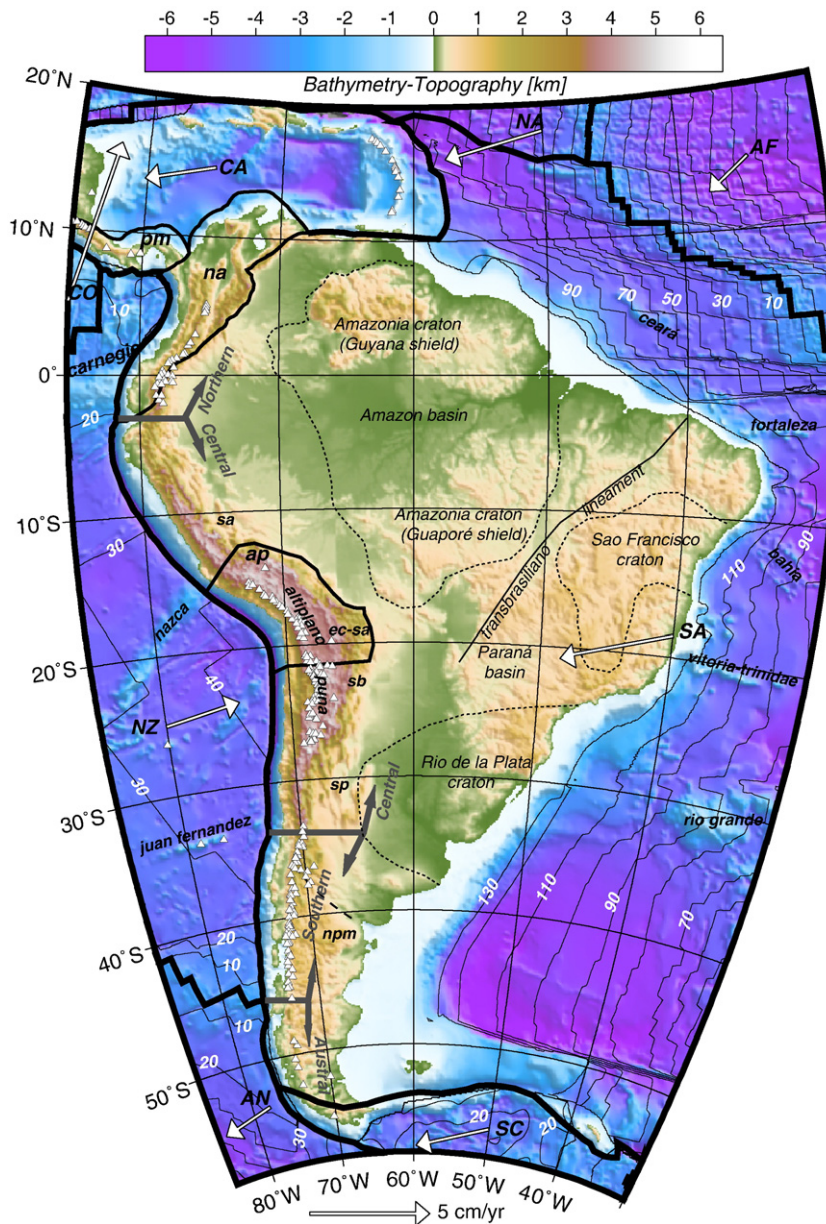The northern and southern margins of the South America plate are right- and left-lateral transform zones

Fig. 1. Geotectonic setting of the study area. Shaded relief image of bathymetry and topography from GEBCO digital data (http://www.ngdc.noaa.gov/mgg/gebco/gebco.html). Thick and thin bold lines are boundaries of large (SA, South America; CA, Caribbean; NA, North America; AF, Africa; SC, Scotia; AN, Antarctica, NZ, Nazca; CO, Cocos) and small (pm, Panama; na, Northern Andes; ap, Altiplano) tectonic plates from model PB2002 (ftp://element.ess.ucla.edu/PB2002) [28]. Arrows depict vectors of plate motion with respect to the hotspot reference frame from model HS3-NUVEL1A [29] as calculated at the given position with the Plate Motion Calculator (http://sps.unavco.org/crustal_motion/dxdt/nnrcalc/). White triangles are active volcanoes (http://www.volcano.si.edu/gvp/world). Diverging grey arrows shows boundaries and names of Andean segments. Dotted lines mark the extent of Achaean to Early Proterozoic cratons. This latter information and the track of the Transbrasiliano Lineament were taken from [30] and [31]. The dashed line oblique to the Southern Andes marks the northern limit of the Patagonian terrain. Over the oceans, thin lines with white numbers mark isochrons of the oceanic lithosphere [32] and names depict major oceanic ridges. Some Andean morphotectonic units are highlighted; Sierras Subandinas (sa), Eastern Cordillera (ec), Santa Barbara System (sb), Sierras Pampeanas, North Patagonian Massif (npm).

accommodating its faster absolute westward movement with respect to the Caribbean and Scotia plates, respectively. This movement is also responsible for the west-

directed polarity of subduction along the Lesser Antilles margin of the Caribbean plate and the Sandwich margin of the Scotia plate. The western margin of the continent has

been tectonically active since at least 500 Ma [37,38]. Its Palaeozoic evolution registers the accretion of terrains to Gondwanaland, but since Jurassic times the active margin has been dominated by east-directed subduction of Pacific oceanic lithosphere. The significant westward acceleration of South America after opening of the Atlantic caused the onset of compressive deformation along its convergent margin that continues during the Cenozoic to form the Andes [38]. This 8000 km long, up to 7000 m high mountain belt shows a strong along-strike morphological segmentation [37–39]. This is characterized by the oroclinal bending of the Altiplano–Puna plateau (after Tibet, the world's second largest continental plateau) around the central part of the margin and decreasing orogenic topography to the north and south [40]. In Fig. 1, the Andean margin is divided into four major segments: Northern (north of 3° S), Central (3°–33° S), Southern (33°–46° S) and Austral (south of 46° S). Based on topography, seismic and geodetic data, Bird [28] proposes the existence of some small plates, the Panamá, Northern Andes and Altiplano plates (Fig. 1), that move as more or less rigid blocks with respect to the South America plate. The eastern boundary between the Altiplano and South America plates corresponds to the active front of the Sierras Subandinas thrust–fold belt, but the northern and southern boundaries gradate to zones of diffuse crustal deformation, called 'orogens' by Bird [28]. The southern tip of South America, known as the Patagonia Platform (Fig. 1), is a geologically distinct lithospheric block with respect to the rest of the continent [37,38,41].

The limits of the Andean segments roughly correlate with the subduction of buoyant oceanic ridges (Carnegie, Nazca, Juan Fernández) that partially control the shape of the subducted slab and therefore the location of active volcanic arcs [42,43]. Slab segments dipping more than 25° favour melting of the asthenospheric wedge that feeds the volcanic zones highlighted in Fig. 1. Volcanic gaps between them are younger than 10 My [37,38] and associated with sub-horizontal, flat segments of the slab at 100–150 km depth [44] that preclude mantle magmagenesis. Active volcanism also occurs along the subduction zones bordering the Panamá plate to the south and the Caribbean plate to the east.

Spreading centres that separate the Nazca plate from the Cocos and Antarctic plates, currently subduct near the northern and southern limbs of the Andean trench. Therefore, the age of the Nazca plate at the trench increases toward the Central Andes, reaching a maximum of 45 My [32]. Aseismic oceanic ridges carried by the Nazca plate toward the subduction zone, as well those occurring on the oceanic part of the South America plate (Río Grande, Vitoria–Trinidade, Bahía, Fortaleza, Ceara), were presumably formed by the interaction of the plate with hot-spots.

3. Spectral isostatic analysis with the fan wavelet method

Spectral isostatic analysis has usually involved generating the admittance (isostatic response function) and/or coherence from Fourier transforms of observed gravity and topography data, and modelling them. One of the simplest models is a uniform elastic plate above an inviscid fluid: the plate flexes under initial surface and subsurface loads and Forsyth [17] showed that these initial loads can be estimated from the observed topography and gravity, given an assumed value of T_e. This allows a model coherence to be calculated, so that T_e can be estimated by minimising the misfit between this and the observed coherence. Use of this 'load deconvolution' [6] implicitly fits the observed admittance and generates the 2D load structure, which is usually expressed as the ratio of subsurface to surface loading as a function of wavenumber $f(k)$, with k being the 2D wavenumber. Typically f increases with wavenumber from $\ll 1$ at small k, to >1 (and sometimes >10) at large k. A simpler alternative to the load deconvolution is to make an assumption about f, for example that it is constant, and use this in the analytic expression for coherence. However, this does not account for the observed admittance or the real loads and, as a result, it does not fit the details of the observed coherence curve. Forsyth [17] shows model coherence curves for $f=1$ which are extremely simple in form, whereas observed coherence curves may show considerable detail due to variation of the loading ratio with wavenumber. Nevertheless, the general form of coherence, i.e. near 1 at long wavelengths (indicating completely compensated topography) passing to near zero at short wavelengths (i.e. elastically supported topography), is almost universal. For typical values of rock properties, the wavelength at which the coherence is 0.5 approximates the flexural wavelength, $\lambda_F \sim 29 T_e^{3/4}$ km [20].

The production of maps showing the spatial variation of T_e is facilitated by using the Continuous Wavelet Transform (CWT) in place of the Fourier transform. The Fourier approach relies on a single T_e estimate being made in a window of fixed size, which is then moved over the study area [4,6,45]. This has the problem that windows smaller than several times the flexural wavelength cannot identify potentially large T_e values, while large windows retrieve an average T_e value and degrade the spatial resolution [4,20]. In contrast, the CWT approach involves the convolution of the entire signal with scaled wavelets, in order to reveal the spectral

characteristics around each data point. In practice, this convolution is performed via the Fourier transform, the wavelet coefficients being the inverse Fourier transform of the product of the Fourier transforms of the signal and the wavelet, at each wavelet scale.

In the approach developed by Kirby and Swain [15], the wavelet coefficients of gridded Bouguer anomaly and topography data are determined using two-dimensional Morlet wavelets arranged at a number of azimuths in a fan geometry [26]. The Morlet wavelet was chosen for the superposition because, being a Gaussian-modulated complex exponential, it is able to reproduce Fourier-derived spectra [24] and hence the analytic formulae for coherence and admittance [15].

To determine the observed wavelet coherence, the auto-spectra of the gravity and topography (Morlet) wavelet coefficients are formed at each azimuth of the fan-geometry, and then averaged. Their ratio is then taken to yield the wavelet coherence [26]. This quantity is isotropic (having been constructed with the fan-geometry), and reveals the coherence at each location (grid node) of the study area. The same procedure can be undertaken for the wavelet admittance.

Inversion of the wavelet coherence, in order to determine T_e at each grid node, can then take two forms. A simple approach [15] is to match the observed wavelet coherence with theoretical coherence curves at each node, while assuming a constant value for the subsurface-to-surface loading ratio, f. More recently, however, Swain and Kirby [26] have developed a wavelet version of Forsyth's approach, in which his loading equations, instead of being applied to the Fourier transforms of gravity and topography, are applied to their (Morlet) wavelet transforms in order to estimate initial surface and subsurface loads given a value of T_e. Averaging the auto- and cross-spectra of these over all the wavelets of the fan, and taking the ratio, yields $f^2(k)$ [15]. From this, a predicted wavelet coherence can be determined (Appendix A2 of Kirby and Swain [25]), and T_e estimated by least-squares minimisation of the predicted coherence against the observed wavelet coherences. We used Brent's method of 1-D minimisation [46] to find the T_e value that gives the best-fitting predicted coherence.

Forsyth's equations assume an initial subsurface load in the form of Moho topography. Deducing this requires the existing Moho relief to be estimated by downward continuation of the Bouguer gravity. This may generate numerical instabilities if the anomalies actually have shallower sources. To avoid this potential difficulty, we use the alternative loading model of Banks et al. [47], which consists of a thin sheet of variable density within the crust. Swain and Kirby [26] also extended this model

to predict the wavelet coherence using the equations given in Appendix A1 of Kirby and Swain [25]. This model requires the depth to the base of the load layer (z_l) and the Moho (z_m) to be specified in addition to crust and mantle densities. The T_e estimates depend very little on z_m or the densities. They do vary with z_l, but this is only significant if T_e is small [17,47]. Note that the two loading models [17,47] give identical results if the load depths coincide (i.e. $z_m = z_l$).

4. Gravity data

Owing to the lack of a gravity dataset with a uniform coverage and resolution over the large area to be studied, we used data from global gravity models derived from the CHAMP and GRACE satellite gravity missions. We tested two recent models that also incorporate terrestrial and marine data, namely the GGM02C [48] and EIGEN-CG03C [27] models. These models are complete to spherical harmonic degree and order 360, which is equivalent to spatial wavelengths of about 105 and 55 km at the northern and southern extremities of our computation region (20° N–60° S). The spherical harmonic coefficients in GGM02C are a weighted combination of the coefficients from the GGM02S (satellite only) model and the older EGM96 (terrestrial/marine) model to degree and order 200 [48]. For higher degrees, coefficients from the EGM96 model are used. In contrast, the coefficients in the EIGEN-CG03C model are derived from CHAMP and GRACE data to degree and order 70, a combination of CHAMP/GRACE and terrestrial/marine data from degree 71 to 120, and are newly computed from terrestrial and marine data between degrees 121 and 360. The overall accuracy of the EIGEN-CG03C model is estimated to be 8 mGal [27].

The global models are available from the International Centre for Global Earth Models (ICGEM, http://icgem. gfz-potsdam.de/ICGEM/ICGEM.html) as 30′ grids of geoid heights or free-air gravity. For both models, we downloaded free-air anomalies globally, extracted data for the South American region, and converted the data to Bouguer anomalies. This conversion involved computing a simple Bouguer correction from GEBCO topography/ bathymetry data (http://www.ngdc.noaa.gov/mgg/gebco/ gebco.html) using an infinite slab with density 2670 kg/m^3 onshore and 1650 kg/m^3 offshore. The Bouguer corrections were low-pass filtered with a cut-off wavelength of 125 km using a Butterworth filter ($n = 8$). This ensures that the Bouguer corrections do not introduce a short-wavelength signal into the calculated Bouguer anomalies, signal which is intrinsically missing in the free-air gravity of the global models. Terrain corrections

were not incorporated, but tests using coarse topographic models show that including terrain corrections changes calculated T_e values by only 1 km on average.

In order to select between the GGM02C and EIGEN-CG03C models, we compared them to terrestrial data in the Central Andes [49]. To extend the comparison to offshore regions, we computed Bouguer anomalies from the KMS2001 altimetry dataset [50]. The results of this comparison (Fig. 2) suggest that, at least for the Central Andes, the EIGEN-CG03C model is a better representation of the surface data. We assume that this comparison is

valid for all of South America and, as a result, use the EIGEN-CG03C model for our T_e calculations. The better comparison between surface data and the EIGEN-CG03C model in the Central Andes probably reflects the fact that the GGM02 model incorporates EGM96 coefficients rather than newly-computed higher-degree coefficients.

5. Results

After applying a Transverse Mercator projection and sampling the data onto 20 km grids, we applied our
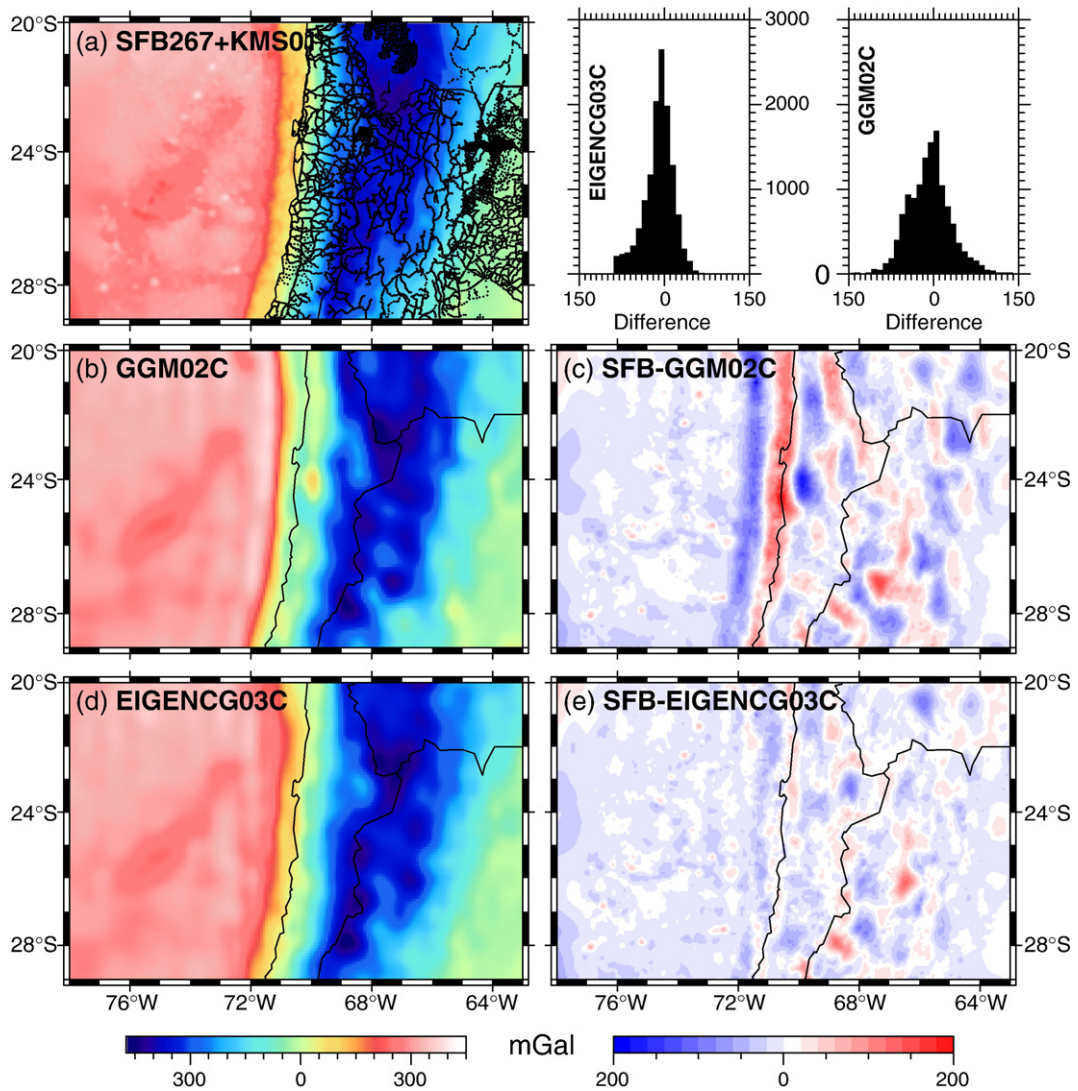

Fig. 2. (a) Terrestrial Bouguer anomalies for the Central Andes from the SFB-267 database [49] and marine anomalies for adjacent oceans from the 2001 version of the KMS satellite altimetry data [50]. Points show the location of onshore measurements. (b) Bouguer anomalies for the same region from the GGM02C model [48]. (c) Differences between the terrestrial/marine data and GGM02C. (d) Bouguer anomalies derived from the EIGEN-CG03C model [27]. (e) Differences between the terrestrial/marine data and EIGEN-CG03C. The difference maps in (c) and (e) and the histograms at top right suggest that the EIGEN-CG03C model is a better representation of gravity anomalies measured at the surface in the central Andean region.

wavelet version of Forsyth's method to the Bouguer gravity derived from the EIGEN-CG03C model and topography/bathymetry data of GEBCO. Water depths were converted to equivalent rock loads [14]. As noted in Section 3, we used a thin sheet model of subsurface loading [47], placing it at a depth (z_1) of 15 km. This is the average depth of the intracrustal density discontinuity separating light upper crustal material from dense lower crust in the 3D density model for the Andean margin of Tassara et al. [51]. Using a value of 10 km for z_1 reduces the smallest T_e values by about 15%, but only 5% on average. For the Moho depth (z_m) we used Crust 2.0 [52]. In fitting the predicted to the observed coherences, we weighted the individual misfits as the inverse of wavenumber [26]; the highest wavenumber of our EIGEN-CG03C Bouguer anomaly is 1/125 km^{-1} (Section 4) and this procedure has the effect of downweighting spurious high coherences that can occur at wavenumbers close to or above this.
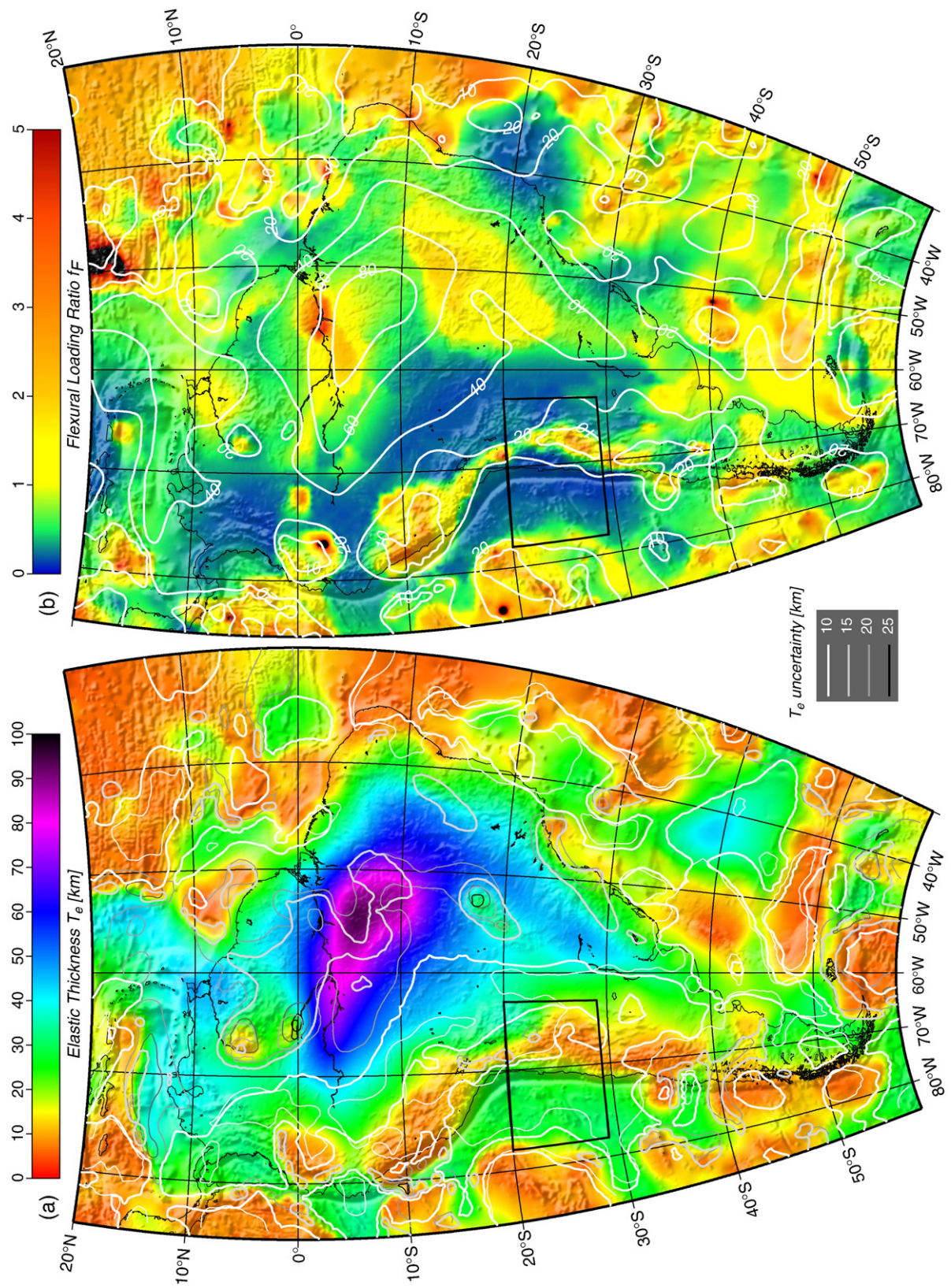
The resulting map of T_e variations is shown in Fig. 3a, which also gives an indication of the uncertainties in T_e. For each point of this map, the estimated T_e value minimises the misfit between observed and predicted coherence. The uncertainties represent the 68% confidence interval around this minimising value [46], but because the misfit curves depend on the weighting, these uncertainties are only crude estimates of the confidence intervals.

As expected from the geological configuration of South America, the elastic thickness is greatest (100 ± 15 km) over the central part of the old Amazonia craton (Guaporé Shield in Fig. 1) and decreases concentrically toward its margins. However, the Guyana Shield, an integral component of Amazonia [30,31], shows T_e as low as 10 km, although with an uncertainty that can reach 25 km. Also significant is a NE–SW corridor of $T_e < 40 \pm 20$ km correlating with the southern track of the Transbrasiliano Lineament. The transform plate boundary between the South America and Caribbean plates shows a relatively high T_e (40 ± 10 km) that also characterizes the southern Lesser Antilles arc. Along the eastern passive margin of continental South America, T_e is lower than 25 ± 15 km, decreasing to less than 10 km in some regions. In contrast to the northern boundary of the continent, the southern transform boundary with the Scotia plate has T_e as low as 5 km in its western part, but with a large uncertainty of 15–20 km. The active, Andean margin of the continent is characterized by the lowest elastic thickness onshore ($T_e < 30 \pm 15$ km) and marked along-strike variations. This variability correlates with the geotectonic segmentation of the Andes. With the exception of

the southern part of the North Patagonian Massif (Fig. 1) and the fore-arc region south of 40° S, most of the Patagonian Platform shows T_e greater than 20 ± 10 km. The northward increase of elevation along the northern part of the Southern Andes correlates with a decrease in T_e to values less than 15 ± 10 km, which characterize most of the Central Andean margin. Here, the zone of $T_e < 15$ km is wider than 250 km along regions north and south of the Altiplano Plateau, encompassing an area from the coastline (or the trench for the northern and southernmost Central Andes) to the eastern boundary of the orogen. In clear contrast to the rest of the weak Central Andes, only the active volcanic arc along the Altiplano segment shows T_e less than 15 km. Here the fore-arc also has the highest T_e of the Central Andes (25 ± 10 km) and the back-arc region seems to be anomalously strong ($T_e \sim 35 \pm 10$ km) compared with the rest of the Central Andean orogen. The southernmost Northern Andes is similar to the Central Andes in having T_e less than 15 ± 10 km, but the boundary between the two Andean segments is clearly marked by a zone where T_e is greater than this value. Northward along the Northern Andes, the elastic thickness increases to values greater than 40 ± 15 km at the junction with the boundary between the South America and Caribbean plates.

Elastic thickness for the oceanic plates shows a great spatial variability. Far away from continental margins, zones of low T_e (less than 15 ± 10 km) broadly correlate with oceanic ridges and spreading centres. Most of the oceanic part of the Africa plate included in our study seems to be uniformly weak ($T_e < 10 \pm 10$ km). The highest T_e values offshore (40 ± 10 km) occur east of the Lesser Antilles trench and to the south of the Río Grande ridge over the deepest region of the South Atlantic basin.

Fig. 3b attempts to map the loading structure resulting from our wavelet-based computations of the elastic thickness. Remember that f, the ratio between subsurface (buried) to surface (topography) loads *prior* to the lithospheric deflection, is a function of both the spatial position and the wavenumber spectrum around a given point. As Forsyth [17] notes, there is a limited bandwidth over which estimates of f have physical significance. We choose to average the values of $f(k)$ for the three wavenumbers near the corresponding flexural wavelength λ_F to define a 'flexural loading ratio' f_F for each (spatial domain) point. In the loading model adopted for this study [47], this parameter approaches one when the load produced by lateral density variations (of unknown magnitude) in an upper-crustal sheet located at a depth $z_1 = 15$ km is similar to the load generated by topographic masses distributed by surface

processes (tectonism, volcanism, erosion). f_F values much lower or higher than one mean that subsurface loads are insignificant or dominant, respectively. The flexural loading ratio depends quite markedly on z_l; reducing it to 10 km decreases the average f_F estimate by 20%. Considering this and the dependence of f_F on λ_F (and hence on T_e), estimates of this parameter should perhaps be more usefully regarded as relative, not absolute values.

The high elastic thickness core of South America is surrounded by regions where $f_F > 1$. Such a region underlies the Amazon basin where f_F reaches values greater than five. In the broader southern region that coincides with the Neoproterozoic mobile belt separating the Amazonia and Sao Francisco cratons, this parameter doesn't exceed two. Despite these and a few other exceptions, most of the areas where $f_F > 1.5$ strongly correlate with zones where elastic thickness is less than 10 km, notably along the margins of the continent and over the oceans. Given that the loading ratio $f(k)$ increases with the wavenumber and that it is inversely correlated with the elastic thickness through the flexural wavelength λ_F, this observation is not surprising. This imposes some restrictions on the interpretation of the spatial variations of f_F shown in Fig. 3b.

5.1. Central Andes

In order to validate our use of the EIGEN-CG03C gravity model for wavelet T_e estimates, we also present a T_e map based on surface data in the Central Andes region (marked by the box in Fig. 3). In this area, the terrestrial/marine gravity data (Section 4, Fig. 2) were projected and gridded at 10 km. Then the data were mirrored at all edges in order to create larger data sets. This has the twin purposes of (a) reducing the downward bias of T_e estimates due to the data extent being comparable to the flexural wavelength and (b) avoiding the edge discontinuities that lead to problems near the data margins due to use of the FFT. Finally, T_e calculations were carried out as for the EIGEN-CG03C data, with the results shown in Fig. 4a. Fig. 4b shows the differences between T_e values computed using the EIGEN-CG03C data (Fig. 3a) and the surface data (Fig. 4a). Note that the EIGEN-CG03C data used in Fig. 4 are those obtained from the entire study area, i.e. without mirroring. This could lead to ambiguity when

interpreting the results in Fig. 4b,c because the terrestrial data were mirrored. However, we re-computed the elastic thickness using a subset of the EIGEN-CG03C data extracted for the Central Andes and mirrored at the edges in the same manner as for the terrestrial/marine data. Using this approach, we found insignificant differences with the results of Fig. 3a. Synthetic models also show that when using the wavelet method, the mirroring procedure does not significantly affect the recovered T_e estimates [14].

Figs. 3a and 4a show a very similar T_e pattern over this area (Fig. 4b). However, over the high cordillera where the lowest elastic thicknesses exist, the surface data predict lower T_e values (<5 km) than the EIGEN-CG03C model (8–10 km). This explains the small peak in the histogram at 6–7 km (Fig. 4c). This difference is hardly surprising given that the EIGEN-CG03C Bouguer data are limited to wavelengths >125 km, which corresponds to the flexural wavelength expected for an elastic thickness of 7 km [20]. Thus, the EIGEN-CG03C data must overestimate T_e where it is less than about 10 km.

6. Discussion

6.1. Comparison with existing T_e estimates

Stewart and Watts [53], Tassara and Yáñez [54] and Tassara [55] estimated the elastic thickness by forward modelling of the gravity field along profiles perpendicular to the western margin of the continent. This kind of modelling fits the observed Bouguer anomaly with that produced by the deflection of the Moho imbedded in a thin elastic plate loaded by the present-day topography. The fitting is achieved in a trial-and-error procedure by iteratively changing the elastic thickness of the plate along the modelled profile. Comparing these previous estimates against our results (Fig. 5), we note a generally good agreement in terms of relative spatial variations. The low T_e determined along the cordillera and higher values toward its flanks are clear for both methods. This is also true for the continental-scale, north–south variations of T_e associated with the Andean segmentation. Of particular interest are the elastic thicknesses in the back-arc–foreland region of the Altiplano: the values that we estimate and those of previous authors are higher in this region than in the orogens to the north and south.

Fig. 3. (a) Computed elastic thickness map (colours) with contours depicting the estimated uncertainty as described in the legend. (b) Computed flexural loading ratio f_F (colours) at the transition coherence wavelength (λ_F) contoured with elastic thickness. Both maps are superimposed on shaded relief. The box outlines the region shown in Fig. 4.
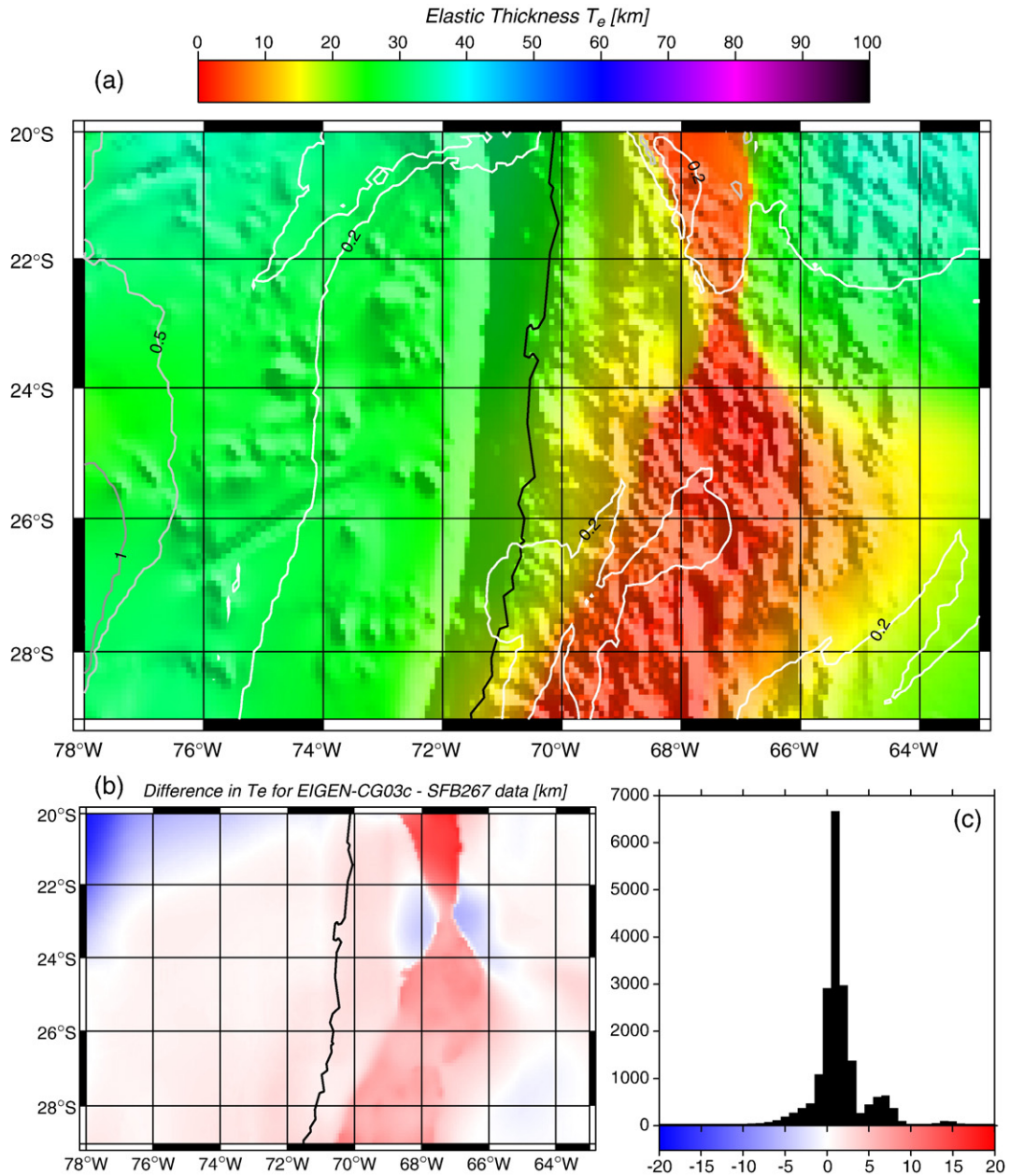
Fig. 4. (a) Results obtained for the Central Andes area (see location in Fig. 3) using terrestrial/marine gravity data (Fig. 2a). The colour map depicts elastic thickness and contours are for the flexural loading ratio f_F. (b) Differences between the elastic thickness estimated from the EIGEN-CG03C gravity model and those from the SFB267+KMS database. (c) Histogram showing the statistical distribution of the differences mapped in (b).

Previous T_e estimates along the Central Andean fore-arc [54,55] agree with our results and show that T_e decreases from the Altiplano region southward. However, the previous estimates are systematically higher (by 30–40 km) than ours. Moreover, T_e estimates of Tassara and Yáñez [54] along the fore-arc reach a maximum south of 40° S, whereas our results show some of the lowest T_e values there. However, high

residual Bouguer anomalies left in the fore-arc region by the modelling of Tassara and Yáñez [54] somehow invalidate the high elastic thicknesses that they determined. It is also significant that these authors subtracted the gravity effect of the subducted slab from the observed Bouguer anomaly prior to modelling. Such a procedure was required to maintain the spatial continuity of the approach they developed, but it

However, we prefer the results produced with the slab gravity effect included in the EIGEN-CG03C Bouguer anomaly. This is because we think that this effect is important in the isostatic balance of the fore-arc and seems to be identified by our method as a loading ratio $f_F > 1$ along the southernmost Southern Andean fore-arc (Fig. 3b).

We note that although the relative spatial variations in T_e agree with previous results, east of the main cordillera our estimates are ~ 50% lower than those derived from forward modelling. In general, the eastward increase in T_e across the back-arc–foreland region is gradual for our results, but relatively sharp for previous T_e estimates. A limitation of the forward modelling approach is that the boundary conditions at one end of the profile (or both ends in the case of Tassara and Yáñez [54]) are such that no deflection is allowed [1,2]. Therefore, the high T_e along the eastern half of these profiles (and the fore-arc region for Tassara and Yáñez [54]) could be an artefact resulting from the forward model setup.

Our results also compare well to those obtained by Ojeda and Whitman [57] for northernmost South America using spectral analysis of windowed topography and gravity data.

6.2. Loading structure

The flexural loading ratio f_F, as defined in this work, is a potential proxy for subsurface mass distribution. However, the strong anti-correlation between f_F and T_e (with flexural loading ratios commonly greater than one for elastic thicknesses less than 15 km) restricts the usefulness of this parameter. This anti-correlation is expected because f_F is an average of $f(k)$ (i.e. the wave-number-increasing ratio between subsurface and surface loads at a given point) around the corresponding flexural wavelength λ_F (i.e. that at which the coherence between topography and gravity approaches $\frac{1}{2}$), which itself defines the elastic thickness. In this context, only regions escaping this anti-correlation can give information on internal lithospheric structure.

The most obvious of these anomalous regions are those below the Amazon basin and the Neoproterozoic belt separating the Amazonia and Sao Francisco cratons and, to a lesser extent, the north-eastern limit of the Amazonia craton and the south-eastern limit of the Rio de la Plata craton. For these regions, f_F is greater than one despite moderate to high T_e. Our results suggest that below these regions there are strong lateral variations in density that are not compensated by surface topography. Previous authors studying the isostatic compensation of the Amazon basin [58], also concluded that anomalously
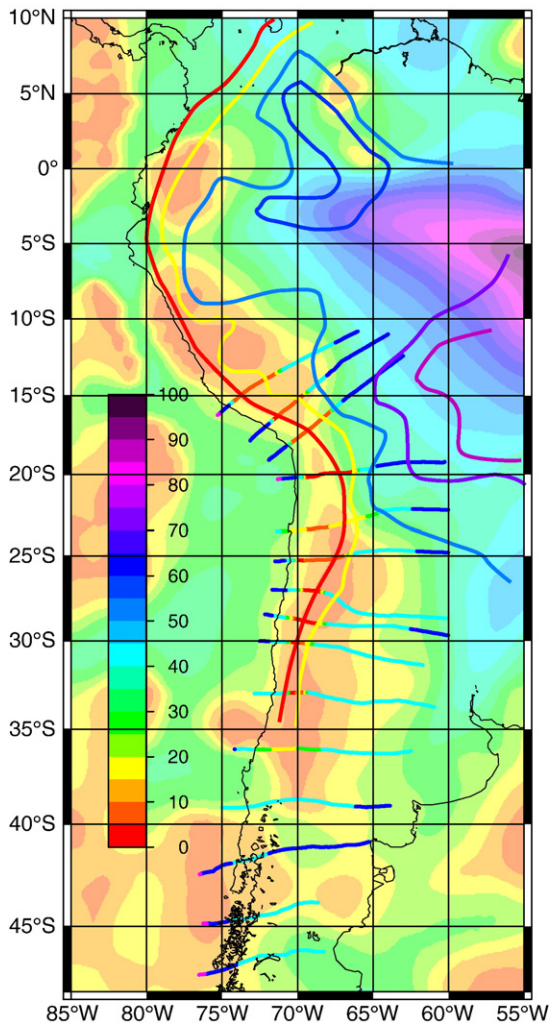

Fig. 5. Comparison between elastic thickness values estimated during this work (colour map) and those reported by Tassara and Yáñez [54], Tassara [55] (coloured trench-normal profiles) and Stewart and Watts [53] (coloured contours). Previous authors estimated T_e by forward modelling the gravity field along profiles perpendicular to the continental margin, but Stewart and Watts [53] presented their results as a contour map. The red line marks the breaking point of the thin elastic plate used by Stewart and Watts [53].

contradicts the accepted notion that the slab participates in the isostatic compensation of the fore-arc [56]. After subtracting the slab gravity effect derived from the 3D density model of Tassara et al. [51] from the EIGEN-CG03C Bouguer anomaly, we re-computed the elastic thickness map and found that T_e increases only along the fore-arc region and especially south of 38° S (to 40–50 km). Owing to the shallow penetration angle of the slab along this latter region [51], this also has the effect of increasing the elastic thickness in the interior of the continent, improving the agreement between our T_e estimates and those of Tassara and Yáñez [54].

dense material should be buried below the thick sedimentary cover in order to explain the gravity anomalies there. In addition to the Amazon basin, two other areas with high f_F are associated with large fluvial basins (Orinoco and Colorado), suggesting that recent erosion and sedimentation were efficient there in removing topographic loads and blanketing relatively large subsurface lateral density variations. The flexural modelling of the Maturín basin of eastern Venezuela [59] suggests the presence of deep buried loads in the form of a slab subducting northward to depths of ~ 200 km. The distribution of seismicity suggests that these deep buried loads spatially coincide with the high-f_F region to the northeast of the Amazonia craton. These regions of the lithosphere are mostly loaded by the stress produced by the uncompensated internal loads that in our approach are assumed to occur at upper-crustal levels. If the actual internal loads are emplaced deeper (i.e. in the lower crust, at the Moho or, as in the case of eastern Venezuela, into the mantle), our method should overestimate the value of f_F. Nevertheless, it gives an interesting indication of the dominance of such loads for some regions and their expected spatial variability.

6.3. Thermal age and elastic thickness

6.3.1. Oceanic plates

It is well accepted that the elastic thickness of oceanic plates is controlled by the thermal age of the lithosphere at the time of loading [1]. T_e estimates obtained by forward modelling and spectral isostatic analysis for a number of oceanic regions worldwide tend to correlate with the depth to the 450 ± 150 °C isotherm predicted from the age of the associated oceanic crust using a simple plate-cooling model [60] with an equilibrium thermal thickness of 125 km [1,61]. This observation and comparisons with yield-strength profiles constructed by extrapolating experimental rheological laws to geological conditions, suggest that T_e approximates the effective thickness of an elastic beam inside the oceanic lithosphere below which peridotitic mantle flows at geological time-scales following a thermally-activated creep law [1,5].

Motivated by these concepts, we sampled our T_e map and the digital isochrons of the world's ocean floor [32] at points every one degree to compare both data with the predictions of a plate-cooling model (Fig. 6a). The large dispersion characterizing this comparison is probably related to the fact that we plot T_e against the actual age of the oceanic crust rather than its age at the time of loading (which is unknown for most oceanic regions). Note that this dispersion could, in fact, be worse. This is because

our data do not resolve elastic thicknesses less than 10 km, which also explains the clustering of T_e around this value. Nevertheless, Fig. 6a shows some interesting observations that warrant discussion. More than 70% of the sampled points plot inside the region enclosed by the depth to the 450 ± 150 °C isotherm. This is more obvious for ages less than 40 My, although some of these young points have T_e values significantly higher than the predicted depth to the 600 °C isotherm. In contrast, elastic thickness for points with ages greater than 70 My tend to be less than the depth to the 450 °C isotherm, with some of them showing T_e values much less than the predicted 300 °C isotherm.

In order to perform a spatial analysis of these tendencies and to search for possible causes, we define the parameter $\Delta T_e = (T_e / Z_{450 \,°C}) \times 100$ as the percentage ratio between the estimated elastic thickness (Fig. 3a) and the age-dependent depth to the 450 °C isotherm predicted by the plate-cooling model for each sampled point. Fig. 7 shows that ΔT_e values between 75% and 125%, which we take to indicate that the estimated elastic thickness is similar to the depth of the 450 °C isotherm, occur only locally in the studied area. This is notably the case for the deep southern Atlantic basin and other oceanic regions away from continental margins. In other areas, obvious anomalous features exist. As mentioned in Section 5.1, our method cannot recover T_e values less than 10 km, which explains why ΔT_e is systematically higher than 200% along active spreading centres where no lithospheric strength is expected. Older oceanic regions with $\Delta T_e > 125\%$ can be observed crossing the North America–South America transform boundary and to the west of the northern Andean trench. The values in the latter area are in agreement with previous observations of anomalously high elastic thickness associated with outer rise regions worldwide [1]. However, most of the Nazca plate along the outer rise off the Central Andes is associated with elastic thicknesses comparable to $Z_{450 \,°C}$, whereas off the Southern and Austral Andes, ΔT_e is less than 75%, suggesting a significant weakening of the oceanic lithosphere approaching the trench. The along-strike variation in the strength of subducting plates could be related to variations in the degree of hydration and serpentinization of the oceanic upper mantle. This is a relatively common process thought to be caused by percolation of seawater through faults parallel to the spreading ridge that are reactivated as the plate bends near the trench [63]. The reason why the plate weakening potentially related to this process seems to be more intense for the Antartic plate and the southern segment of the Nazca plate is not obvious to us, but could be due to the young oceanic lithosphere of these plates that enhances
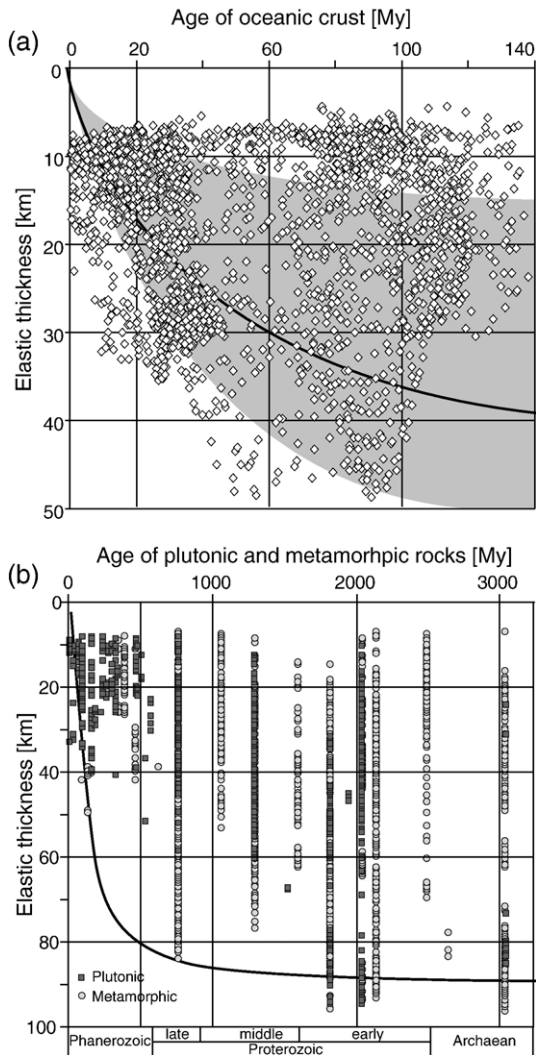
Fig. 6. (a) Elastic thickness versus age of the oceanic crust [32]. The bold line is the 450 °C isotherm predicted by a plate-cooling model [60] for a thermal thickness of 125 km. The grey shading marks the region between the 300 °C and 600 °C isotherms. (b) Elastic thickness versus the mean age of igneous and metamorphic rocks as reported in the digital geological map of South America [62]. The bold line is the 450 °C isotherm predicted by a plate-cooling model with a thermal thickness of 250 km.

the potential for bending at the trench. We note that these segments of the Nazca and Antarctic plates are profusely disrupted by fracture zones emanating from the Chile Rise spreading centre, which could also help to weaken the plate via mechanical fracturing and mantle hydration.

For large areas of the study region, oceanic T_e is much lower than the predicted 450 °C isotherm (Fig. 6a). $\Delta T_e < 50\%$ is characteristic of aseismic ridges and should be caused by the thermal rejuvenation of oceanic plates after interacting with deep thermal anomalies like

hotspots. In addition, the loads produced by this interaction (surface volcanism, subsurface intrusions and thermally-induced mantle density changes) were emplaced for some of these ridges early in the thermal evolution of the oceanic plate and our T_e estimates should represent the hotter-than-today thermal state of the plate at the time of loading. Low strength inherited after the continental rifting that separated South America and Africa can similarly explain the low elastic thickness estimated for the oldest oceanic part of the South America plate along the eastern continental margin, where ΔT_e can be less than 25%. This has also been observed along other passive margins [4,14,64] and explained by the fossilization, as the lithosphere cools, of the loading structure and the low elastic thicknesses characteristically associated with the rifting process [64]. The oceanic part of the Africa plate analysed in this study seems to be significantly weaker ($\Delta T_e < 25\%$) than its South American counterpart. The anomalously low elastic thickness over this region correlates with low seismic velocities at depths of 120–400 km [65] that characterize the region to the east of the Mid Atlantic Ridge north of 0° S. Low seismic velocities at upper mantle depth are primarily caused by high temperatures [66] that, in this case, could be related to the Cape Verde plume [67].

6.3.2. South American continent

The relationship between elastic thickness and the age of the continental lithosphere is less clear than for oceanic plates. As noted by several authors, T_e estimates of continental areas show a wide range of values defining a weak bimodal distribution with peaks near 20 and 80 km and no obvious correlation with the age of rocks exposed at the surface [1,3]. This is primarily the consequence of the complex rheological structure of crust and mantle that results from the wide range of tectonic processes that have affected the compositionally heterogeneous continental lithosphere during long geological times. The thermal structure is only one factor controlling the strength of the continental lithosphere. The compositional structure (depth to the Moho and internal crustal discontinuities) and tectonic stress regime are also significant for the integrated strength of continents [3,5,10]. For instance, the potential mechanical decoupling between weak crust and strong mantle that can occur after sufficient crustal thickening, is thought to be responsible for the low T_e values defining the 20 km peak in the global compilation of continental elastic thickness [1,3].

As for the oceanic lithosphere, we compare in Fig. 6b our T_e estimates with the age of crystalline rocks outcropping over the South American continent. These ages were extracted from the digital geological map of
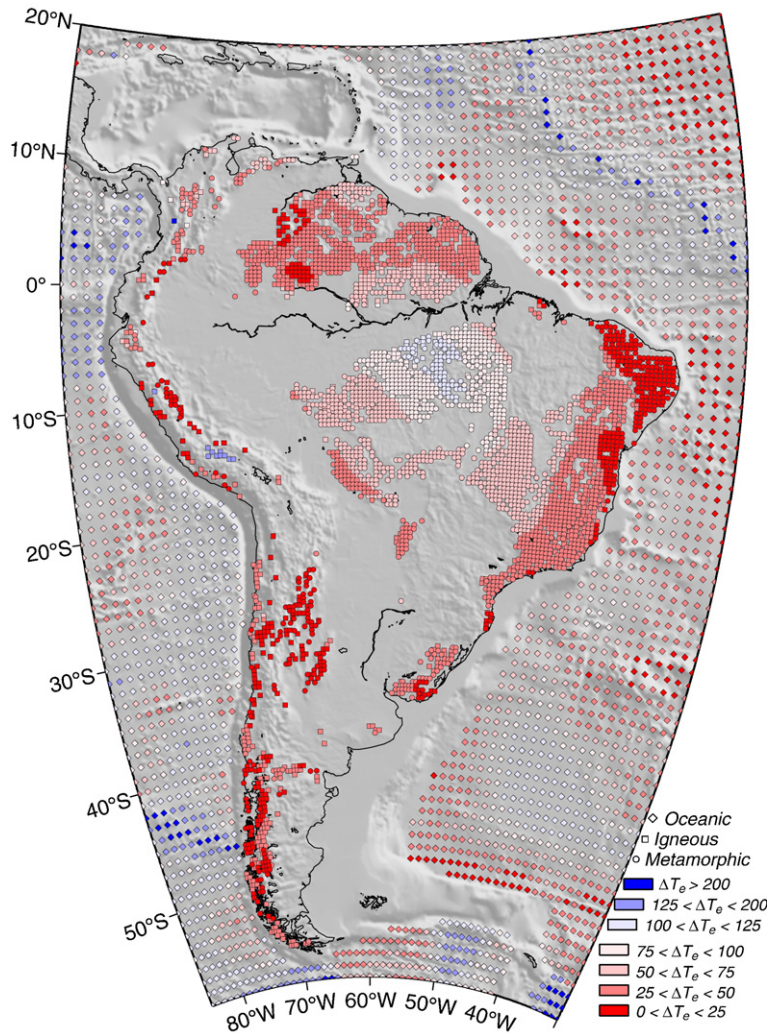
Fig. 7. Map showing the spatial distribution of ΔT_e, i.e. the percentage difference between the estimated elastic thickness and the depth to the 450 °C isotherm predicted by a plate-cooling model from the age of oceanic crust (diamonds), and igneous (squares) and metamorphic (circles) rocks on the continent. The equilibrium thermal thickness of the plate-cooling model is 125 km for the oceanic plates and 250 km for the continent. Blue and red colours respectively refer to the case in which T_e is higher and lower than the age-predicted depth to the 450 °C isotherm.

South America [62] after gridding the average age of igneous and metamorphic bodies (assumed to show the age of crustal formation) and resampling every 15′. Owing to the continental scale of this database, these averages commonly have a large uncertainty of 30–50%. Fig. 6b also includes the depth to the 450 °C continental isotherm predicted by the age-dependent plate-cooling model with an equilibrium thermal thickness of 250 km. This high thermal thickness is more representative of the continental thermal structure [1,3,2] and produces a rapid increase of $Z_{450 \text{ °C}}$ as the lithosphere becomes older, reaching an asymptotic value near 90 km for ages greater than 1 Gyr. The depth to this isotherm is an upper bound on the elastic thickness and the majority of points

analysed in Fig. 6b have T_e values much lower than the corresponding $Z_{450 \text{ °C}}$. This could be partially due to the uncertainties in the age of crystalline rocks, but we think it is a robust feature demonstrating that the thermomechanical structure of the South American lithosphere has been strongly modified by Phanerozoic tectonic processes.

To study this observation, we used the plate-cooling model to compute the depth to the 450 °C continental isotherm predicted from the age of each sampled point and then the percentage ratio between estimated elastic thickness and this depth (ΔT_e), as for the oceanic case. The values of this parameter are also mapped in Fig. 7. This map shows that the central part of the Amazonia craton (south of the Amazon basin) is the only portion of

South America where the estimated elastic thickness corresponds (within a 25% confidence range) to the depth of the 450 °C expected from the age of outcropping rocks. This result suggests that this region in the centre of the continent has been protected from the thermotectonic processes that affected its margins after the Archaean–Palaeoproterozic accretion of the craton. The weakening produced by such processes seems to increase gradually and concentrically away from the Guaporé Shield, at least toward the passive eastern margin where the dominance of crystalline rocks at the surface allows a good sampling. Along this margin, ΔT_e values systematically less than 50% indicate that the Mesozoic rifting process was very efficient here in reducing the strength of Gondwana prior to its desegregation. Extreme weakening ($\Delta T_e < 25\%$) characterizes the eastern tip of the continent and locally the western part of the Guyana Shield. The former seems to coincide with the major triple junction from which the continental rifting is supposed to have started expanding during the Cretaceous [35] and also with the weakest oceanic region of the South America plate (i.e. between the Bahía and Fortaleza oceanic ridges). This suggests that the very low elastic thickness onshore is caused by a longer thermal connection to mantle plumes. The weak spots of the Guyana Shield lie at the westernmost extent of an east–west band of relatively low T_e that is remarkably correlated with a mapped structural corridor (Fig. 8) that disembogues in a weak region of the oceanic plate. This corridor has been proposed to be a failed arm of the rift system separating South America from Africa [35] and the weak spots at its western end could be related to some localized thermal influence from mantle plumes at the beginning of this process.

Although less intense, the western outcropping boundary of the Guaporé Shield also shows a significant weakening ($25\% < \Delta T_e < 50\%$) that, in this case, could be partially due to the Neoproterozoic Sunsas orogeny that affected this part of the old craton [31], but it could also have been influenced by the much younger Andean orogeny. This active orogeny is responsible for the substantial weakening observed for most of the Central, Southern and Austral Andes. This weakening is extreme for Neoproterozoic to Early Palaeozoic rocks forming the Sierras Pampeanas (see Fig. 1) and the core of the Peruvian cordillera, and more localized along some regions of the Southern and Austral volcanic zones whose basement is formed by Mesozoic batholiths. The Northern Andes are comparatively less weak than the rest of the Andean margin with ΔT_e values increasing northward to more than 50% and as high as 150%, as sampled by some Precambrian rocks in the fore-arc region. Points with ΔT_e values between 125% and 200%

in the northern boundary of the Altiplano correspond with exhumed Neogene plutons, for which the plate-cooling model predicts a $Z_{450 °C}$ of 10 km that, if defining the elastic thickness, cannot be recovered by our approach.

The overall low elastic thickness along the Andean margin is a consequence of several factors, including high temperatures induced by the thermal convection of the mantle wedge, extensive mantle hydration by slab-derived fluids, high degrees of mantle and crustal partial melting along active volcanic arcs and possibly also remaining in recent volcanic gaps, high crustal thickness producing the decoupling of crust and mantle, and high tectonic stresses related to plate convergence. Along-strike variations in the elastic thickness should be related to systematic spatial variations in these factors, and a deeper understanding of their nature and potential interaction could be gained by performing a quantitative analysis of our results in the future.

6.4. Strength, earthquakes and neotectonics

Some authors have recognized that the strength contrast between different lithospheric domains could control the localization of deformation in response to tectonic forces and potentially the distribution of earthquakes [6,68]. Therefore, independently of the vigorous debate on the physical link between elastic thickness and seismicity of the continental lithosphere [69–72], a high resolution map of the elastic thickness could be a useful tool for analysing neotectonics and seismogenesis.

In order to evaluate this potential, in Fig. 8 we have plotted the elastic thickness map of our study area together with surface faults and earthquake epicentres of shallow origin (<50 km depth). The seismicity database (see caption to Fig. 8) is based on data recorded at teleseismic distances and is restricted to seismic magnitudes (Mb) between 3.4 and 8.2 for the time period 1964 to 2004. Therefore, it is an incomplete snapshot of the seismic activity in the study region. Similarly, the digital geological map of South America [62] does not distinguish between old, largely inactive faults and neotectonic structures. Moreover, we suspect that the spatial variations in the density of mapped structures could partially reflect differences in the accuracy with which several compilers digitized faults from sources of varying detail and quality to produce this continental-scale map. With consideration of the limits imposed by these restrictions, we note some interesting features that are revealed by Fig. 8.

The boundary of the high-strength core of the continent ($T_e \sim 70$ km) is marked by at least three points where
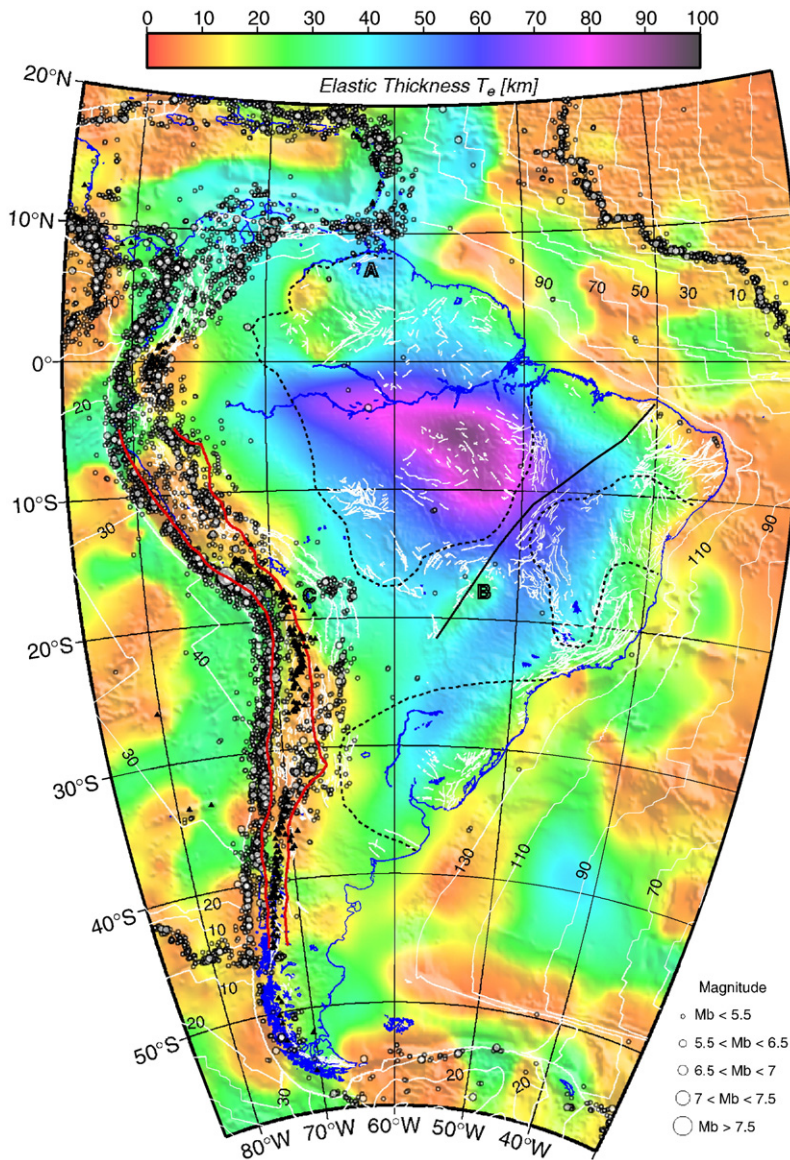
Fig. 8. Elastic thickness map for South America and surrounding regions overlain by seismicity and surface structures. Circles mark earthquake epicentres for events shallower than 50 km taken from: the PDE–NEIC catalogue (http://neic.usgs.gov/neis/epic/epic.html) for magnitudes 3.4<Mb<5.5 and the period 1973–2004; Engdahl et al., [73] for magnitudes 4<Mb<8.2 and the period 1964–2004 (A. Villaseñor, pers. comm.). Red lines show the 50 and 150 km contours of the subducted slab [51] and white lines show faults from the digital geological map of South America [62]. Capital letters are referenced in the main text. Lineaments and the boundaries of cratons are as in Fig. 1.

seismic activity does exist and is of small to intermediate magnitude (Mb<6.5). This boundary, which also correlates with some surface structures, could be a region of active lithospheric deformation at the craton margins. Alternatively, we observe that these regions of active seismicity, as well as those near the north-eastern margin of the Guyana Shield (A in Fig. 8), seem to be dominated by subsurface loads (f_F>1 in Fig. 3b) and hence could be associated with the release of stresses supporting density anomalies located within the crust or deeper in the mantle. Owing to the high

stresses that are necessary to produce brittle failure at these depths [71], seismicity below these regions probably occurs in association with mechanical disconti-nuities connecting zones of contrasting density structure.

The south-western track of the Transbrasiliano Lineament (B in Fig. 8) is marked by a zone where the elastic thickness is less than 40 km, in clear contrast to the strong surrounding domains. The northern boundary of this relatively weak zone shows indications of small magnitude seismicity, which is confirmed as a region of

concentration of seismic activity by data compiled from local sources [33]. The Transbrasiliano Lineament is interpreted as a Meso-Neoproterozoic megasuture between the old Amazonia and Sao Francisco cratons [31,35] and our results demonstrate that this structure has remained considerably weak for the last 1 Gyr, helping to release the current tectonic stresses accumulated in the interior of the continent. The weakening associated with this structure, most obvious at its southern end, could have been enhanced during the Mesozoic by the penetration of mantle plumes that left low seismic velocity anomalies at 150–200 km depth, as observed in seismic tomography models [33,36].

Intense shallow seismicity in the active Andean margin of South America is associated with two fundamentally distinct processes. To the west of the 50 km slab-depth contour, which roughly coincides with the coastline (Fig. 8), seismogenesis is mostly caused by the release of stresses accumulated along the elastically locked zone of the subduction interface. To the east of this line, intraplate seismicity commonly occurs within the upper–middle crust in response to neotectonic activity and partially absorbs the portion of the convergence that is not released by subduction earthquakes. All along the Central and Southern Andes the intraplate seismicity tends to be localized in the weak zone where the elastic thickness is less than 15 km. There is a significant concentration of seismicity and higher seismic magnitudes along the faults defining the eastern limit of this zone. The correlation between crustal seismicity, low strength, high topography and thick crust (>60 km [51]) along most of the Central Andes suggests that a weak lithosphere allows the simultaneous action of brittle upper-crustal deformation that produces seismicity and deeper crustal and mantle processes. This coupling leads to permanent deformation and the development of orogenic topography via crustal thickening. However, we are intrigued by the relatively high T_e that characterizes the back-arc of the Altiplano Plateau (C in Fig. 8), the widest and thickest [51] part of the Andean cordillera. Compared with the orogens to the north and south, this region is also anomalous in that it exhibits almost no seismicity below the high and flat topography and a strong concentration of seismic activity in the eastern tip of the active fold–thrust belt of the Sierras Subandinas. What distinguishes the Altiplano from the rest of the Central Andes is that the upper crust is not accumulating compressive deformation and it seems to be mechanically disconnected from the rest of the lithosphere, which here should be formed by the western extent of the rigid Brasilian Shield being thrust under the cordillera [74,75]. Receiver function studies and deep-seismic reflection experiments [76,77] recognize a

notorious discontinuity 20–25 km below the Altiplano that could act as an efficient decollement connecting the eastern active boundary of the Sierras Subandinas with the base of the Altiplano upper crust. Hot and weak lower crust below this decollement could be forced to flow laterally toward the north and south in response to the underthrusting of the rigid Brasilian Shield from the east and the confinement produced by the strong fore-arc ($T_e \sim 25$ km) to the west [55]. Such lower crustal flow has also been advocated to explain the bulk mass distribution and upper-crustal deformation along the plateau [78,79].

For the first time, our T_e map illustrates, with high resolution, the spatial variations in strength along an active subduction zone. Owing to the lack of knowledge of the potential relationship between great subduction earthquakes and elastic thickness, and the incompleteness of the seismic database used for this work, we choose to avoid significant interpretation at this stage. However, the variations in T_e near the trenches included in our study (Fig. 8) seem to be strongly correlated with a seismogenic segmentation of the subduction zone. This suggests that the integrated long-term strength of the coupled slab–fore-arc system, as revealed by our elastic thickness map, should be an important control on the earthquake frequency and magnitude distribution along the seismogenic zone and, hence, on the potential predictability of destructive earthquakes. This correlation should be carefully analysed in the future with the aim to search for possible causes of the correlation and to improve our understanding of seismogenic processes in subduction zones. The methods applied here would then be useful for the assessment of seismic and tsunami hazard along the Andean margin and other fore-arcs worldwide.

7. Conclusions

As also shown by Swain and Kirby [26] for Australia, the fan wavelet version of Forsyth's spectral isostatic analysis is very efficient in recovering the continental- to regional-scale distribution of elastic thickness (T_e) over a wide range of tectonic environments. For our study, this includes the old core of the South American continent and its transform, passive and active margins, as well as several oceanic plates of different ages that have been diversely affected through interaction with hotspots and subduction zones. The method is also able to give significant information on the mass distribution within the lithosphere through interpretation of the flexural loading ratio (f_F).

We demonstrated that a simple Bouguer correction applied to the global free-air gravity model EIGEN-CG03C, which combines terrestrial/marine data and data

from the CHAMP and GRACE satellite missions [27], produces a homogeneous Bouguer anomaly map for the vast region studied. The derived Bouguer anomaly map compares well with terrestrial/marine data independently acquired over the Central Andes and is suitable for the calculation of T_e when it is greater than 10 km. Considering that this global gravity model is freely available (http://icgem.gfz-potsdam.de/ICGEM/ICGEM.html), we think that the methods presented here could be successfully applied to investigate the rigidity structure over most of the continents and oceanic basins of the Earth.

The resulting f_F map shows that internal loads can be significantly larger than topographic loads in regions like the fluvial basins that cover the old east and central part of the continent and intracontinental subduction zones like the one proposed for eastern Venezuela. Some of these regions seems to be correlated with seismicity clusters at crustal depths (<50 km), suggesting that the stress produced by lateral density variations within the continental lithosphere could be released by crustal earthquakes. Inspecting the incomplete seismicity catalogue used for this work (Fig. 8), we note that some of these earthquakes can have magnitudes as high as Mb 6.5, representing a potential risk for nearby populations. Our results, together with more precise seismic data and a better understanding of the relationship between internal crustal stresses due to buried masses and their seismic release along associated mechanical discontinuities, should help to evaluate the seismic hazard in these regions.

We analysed the elastic thickness structure in the framework of an age-dependent plate-cooling model for oceanic and continental plates and demonstrated that only some oceanic regions preserve the thermal structure derived from the secular cooling after plate creation at spreading centres. Most of the oceanic lithosphere surrounding South America has been thermomechanically weakened through interaction with known hotspots and locally by fracturing and serpentinization near deep-sea trench axes. Similarly, the rifting of Africa and South America, strike–slip motions along the northern and southern plate boundaries and the long history of subduction and orogeny along the western margin of South America, have profoundly reduced the strength of the continental lithosphere. Only a strong core protected at the interior of the continent has resisted the thermomechanical influence of these Phanerozoic events.

Along-strike variations in T_e along the western edge of the continent correlate with the geotectonic segmentation of the Andean margin and with the pattern of crustal seismicity. In particular, most of the high and thick Central Andean orogen is characterized by T_e less than 15 km and by shallow intraplate seismicity. This suggests that very weak lithosphere promotes crustal thickening via diffuse deformation at all crustal levels. Notably, the Altiplano segment (the highest, widest and thickest region of the Andes) has a higher elastic thickness in the back-arc (35 km) than the rest of the Central Andes and crustal seismicity does not occur below the high elevations, but instead occurs to the east at the outer edge of the fold-and-thrust belt. This suggests a fundamentally different deformation mechanism that is most likely related to the westward underthrusting of the Brasilian shield below an upper-crustal decollement that separates the rigid upper crust from lower-crustal flow.

Finally, our method has, for the first time, mapped the rigidity structure along the continent–ocean transition over a seismically active subduction zone. Comparing this structure with the distribution of earthquakes along the interplate fault, we observe an interesting spatial correlation in which seismic gaps exist where the slab–fore-arc system seems to be significantly weak ($T_e < 15$ km). Owing to the intrinsic incompleteness of the analysed seismicity catalogue, it is difficult at present to propose a physical link between both observations. However, we think that the correlation between the rigidity structure and seismogenic segmentation along the subduction fault suggests a causal relationship that should be investigated in order to improve the understanding and predictability of great earthquakes and tsunamis along the highly-populated Andean margin and other margins worldwide.

Acknowledgement

References

[1] A.B. Watts, Isostasy and Flexure of the Lithosphere, Cambridge University Press, Cambridge, 2001 458 pp.

[2] D. Turcotte, G. Schubert, Geodynamics, 2nd edition, Cambridge University Press, 2002 456 pp.

[3] E. Burov, M. Diament, Isostasy, equivalent elastic thickness, and inelastic rheology of continents and oceans, Geology 24 (5) (1996) 419–422.

[4] M. Pérez-Gussinyé, A.R. Lowry, A.B. Watts, I. Velicogna, On the recovery of the effective elastic thickness using spectral methods: examples from synthetic data and the Fennoscandian shield, J. Geophys. Res. 109 (2004) B10409, doi:10.1029/2003JB002788.

[5] C. Goetze, B. Evans, Stress and temperature in the bending lithosphere as constrained by experimental rock mechanics, Geophys. J. R. Astron. Soc. 59 (1979) 463–478.

[6] A.R. Lowry, R.B. Smith, Strength and rheology of the western U.S. Cordillera, J. Geophys. Res. 100 (B9) (1995) 17,947–17,963.

[7] S.A.P.L. Cloetingh, E.B. Burov, Thermomechanical structure of European continental lithosphere: constraints from rheological profiles and EET estimates, Geophys. J. Int. 124 (1996) 695–723.

[8] L.L. Lavier, M. Steckler, The effect of sedimentary cover on the flexural strength of continental lithosphere, Nature 389 (1997) 476–479.

[9] K.-F. Ma, T.-R.A. Song, Thermo-mechanical structure beneath the young orogenic belt of Taiwan, Tectonophysics 388 (2004) 21–31.

[10] M. Pérez-Gussinyé, A.B. Watts, The long-term strength of Europe and its implications for plate-forming processes, Nature 436 (2005) 381–384.

[11] M.S.M. Mantovani, S.R.C. de Freitas, W. Shukowsky, Tidal gravity anomalies as a tool to measure rheological properties of the continental lithosphere: application to the South American Plate, J. South Am. Earth Sci. 14 (1) (2001) 1–14.

[12] C. Braitenberg, J. Ebbing, H.-J. Götze, Inverse modelling of elastic thickness by convolution method—the eastern Alps as a case example, Earth Planet. Sci. Lett. 202 (2002) 387–404.

[13] F.J. Simons, R.D. van der Hilst, M.T. Zuber, Spatiospectral localization of isostatic coherence anisotropy in Australia and its relation to seismic anisotropy: implications for lithospheric deformation, J. Geophys. Res. 108 (B5) (2003) 2250, doi:10.1029/2001JB000704.

[14] C.P. Stark, J. Stewart, C.J. Ebinger, Wavelet transform mapping of effective elastic thickness and plate loading: validation using synthetic data and application to the study of southern African tectonics, J. Geophys. Res. 108 (B12) (2003) 2558, doi:10.1029/2001JB000609.

[15] J.F. Kirby, C.J. Swain, Global and local isostatic coherence from the wavelet transform, Geophys. Res. Lett. 31 (2004) L24608, doi:10.1029/2004GL021569.

[16] T.A. Jordan, A.B. Watts, Gravity anomalies, flexure and the elastic thickness structure of the India–Eurasia collisional system, Earth Planet. Sci. Lett. 236 (2005) 732–750.

[17] D.W. Forsyth, Subsurface loading and estimates of the flexural rigidity of continental lithosphere, J. Geophys. Res. 90 (1985) 12623–12632.

[18] D. McKenzie, J.D. Fairhead, Estimates of the effective elastic thickness of the continental lithosphere from Bouguer and free air gravity anomalies, J. Geophys. Res. 102 (B12) (1997) 27,523–27,552.

[19] D. McKenzie, Estimating T_e in the presence of internal loads, J. Geophys. Res. 108 (B9) (2003) 2438, doi:10.1029/2002JB001766.

[20] C.J. Swain, J.F. Kirby, The effect of noise on estimates of the elastic thickness of the continental lithosphere by the coherence method, Geophys. Res. Lett. 30 (11) (2003) 1574, doi:10.1029/2003GL017070.

[21] P. Audet, J.-C. Mareschal, Variations in elastic thickness in the Canadian Shield, Earth Planet. Sci. Lett. 226 (2004) 17–31.

[22] R. Rajesh, D.C. Mishra, Lithospheric thickness and mechanical strength of the Indian shield, Earth Planet. Sci. Lett. 225 (2004) 319–328.

[23] P. Flück, R.D. Hyndman, C. Lowe, Effective elastic thickness t_e of the lithosphere in western Canada, J. Geophys. Res. 108 (2003) 2430, doi:10.1029/2002JB002201.

[24] J.F. Kirby, Which wavelet best reproduces the Fourier power spectrum? Comput. Geosci. 31 (7) (2005) 846–864.

[25] J.F. Kirby, C.J. Swain, Mapping the mechanical anisotropy of the lithosphere using a 2D wavelet coherence, and its application to Australia, Phys. Earth Planet. Inter. 158 (2–4) (2006) 122–138.

[26] C.J. Swain, J.F. Kirby, An effective elastic thickness map of Australia from wavelet transforms of gravity and topography using Forsyth's method, Geophys. Res. Lett. 33 (2006) L02314, doi:10.1029/2005GL025090.

[27] C. Förste, F. Flechtner, R. Schmidt, U. Meyer, R. Stubenvoll, F. Barthelmes, R. König, K. Neumayer, M. Rothacher, C. Reigber, R. Biancale, S. Bruinsma, J.-M. Lemoine, J. Raimondo, A new high resolution global gravity field model derived from combination of GRACE and CHAMP mission and altimetry/gravimetry surface gravity data, General Assembly of the European Geosciences Union, European Geosciences Union, Vienna, Austria, 2005.

[28] P. Bird, An updated digital model of plate boundaries, Geochem. Geophys. Geosyst. 4 (3) (2003) 1027, doi:10.1029/2001GC000252.

[29] A.E. Gripp, R.G. Gordon, Young tracks of hotspots and current plate velocities, Geophys. J. Int. 150 (2002) 321–361.

[30] U. Cordani, K. Sato, Crustal evolution of the South American Platform, based on Nd isotopic systematics on granitoid rocks, Episodes 22 (3) (1999) 167–173.

[31] A. Kröner, U. Cordani, African, southern Indian and South American cratons were not part of the Rodinia supercontinent: evidence from field relationships and geochronology, Tectonophysics 375 (1–4) (2003) 325–352.

[32] R. Müller, W. Roest, J.-Y. Royer, L. Gahagan, J. Sclater, Digital isochrons of the worlds ocean floor, J. Geophys. Res. 102 (1997) 3211–3214.

[33] M. Assumpção, M. Schimmel, C. Escalante, J. Roberto Barbosa, M. Rocha, L.V. Barros, Intraplate seismicity in SE Brazil: stress concentration in lithospheric thin spots, Geophys. J. Int. 159 (1) (2004) 390–399.

[34] J.C. VanDecar, D.E. James, M. Assumpção, Seismic evidence for a fossil plume beneath South America and implications for plate driving forces, Nature 378 (1995) 25–31.

[35] J. Jacques, A tectonostratigraphic synthesis of the Sub-Andean basins: inferences on the position of South American intraplate accommodation zones and their control on South Atlantic opening, J. Geol. Soc. 160 (5) (2003) 703–717.

[36] M. Schimmel, M. Assumpção, J. VanDecar, Seismic velocity anomalies beneath SE Brazil from P and S wave travel time inversions, J. Geophys. Res. 108 (B4) (2003) 2191, doi:10.1029/2001JB000187.

[37] C. Mpodozis, V.A. Ramos, The Andes of Chile and Aargentina, in: G.G. Ericksen, M.M. Cañas Pinochet, J. Reinemund (Eds.), Geology of the Andes and its relation to hydrocarbon and mineral resources, Earth Science Series, Circum-Pacific Council of Energy and Mineral Resources, Houston, Texas, 1989, pp. 59–89.

[38] V.A. Ramos, Plate tectonic setting of the Andean Cordillera, Episodes 22 (3) (1999) 183–190.

[39] A. Gansser, Facts and theories on the Andes, J. Geol. Soc. (Lond.) 129 (1973) 93–131.

[40] B.L. Isacks, Uplift of the Central Andean Plateau and bending of the Bolivian orocline, J. Geophys. Res. 93 (B4) (1988) 3211–3231.

[41] W. von Gosen, Thrust tectonics in the North Patagonian Massif (Argentina): implications for a Patagonia plate, Tectonics 22 (1) (2003) 1005, doi:10.1029/2001TC901039.

[42] T.E. Jordan, B.L. Isacks, R.W. Allmendinger, J.A. Brewer, V.A. Ramos, C.J. Ando, Andean tectonics related to geometry of subducted Nazca plate, Geol. Soc. Amer. Bull. 94 (1983) 341–361.

[43] M.-A. Gutscher, W. Spakman, H. Bijwaard, R. Engdahl, Geodynamics of flat subduction: seismicity and tomographic

constraints from the Andean margin, Tectonics 19 (2000) 814–833.

[44] T. Cahill, B.L. Isacks, Seismicity and shape of the subducted Nazca plate, J. Geophys. Res. 97 (B12) (1992) 17,503–17,529.

[45] M.T. Zuber, T.D. Bechtel, D.W. Forsyth, Effective elastic thicknesses of the lithosphere and mechanisms of isostatic compensation in Australia, J. Geophys. Res. 94 (7) (1989) 9353–9367.

[46] W.H. Press, B. Flannery, S. Teukolsky, W. Vetterling, Numerical Recipes in FORTRAN 77, Cambridge University Press, 1992 992 pp.

[47] R.J. Banks, S. Francis, R. Hipkin, Effects of loads in the upper crust on estimates of the elastic thickness of the lithosphere, Geophys. J. Int. 145 (2001) 291–299.

[48] B. Tapley, J. Ries, S. Bettadpur, D. Chambers, M. Cheng, F. Condi, B. Gunter, Z. Kang, P. Nagel, R. Pastor, T. Pekker, S. Poole, F. Wang, GGM02 — an improved Earth gravity model from GRACE, J. Geod. 79 (2005) 467–478.

[49] S. Schmidt, H.-J. Götze, Bouguer and isostatic maps of the central Andes, in: O. Oncken, G. Chong, G. Franz, P. Giese, H.-J. Götze, V. Ramos, M. Strecker, P. Wigger (Eds.), The Andes — Active Subduction Orogeny, Frontiers in Earth Science Series, vol. 1, Springer-Verlag, Berlin, 2006, pp. 559–562.

[50] O.B. Andersen, P. Knudsen, Global marine gravity field from the ERS-1 and GEOSAT geodetic mission altimetry, J. Geophys. Res. 103 (C4) (1998) 8129–8138.

[51] A. Tassara, H.-J. Götze, S. Schmidt, R.I. Hackney, Three-dimensional density model of the Nazca plate and the Andean continental margin, J. Geophys. Res. 111 (2006) B09404, doi:10.1029/2005JB003976.

[52] C. Bassin, G. Laske, T.G. Masters, The current limits of resolution for surface wave tomography in North America, EOS Transactions AGU 81 (2000) F897.

[53] J. Stewart, A.B. Watts, Gravity anomalies and spatial variations of flexural rigidity at mountain ranges, J. Geophys. Res. 102 (B3) (1997) 5327–5352.

[54] A. Tassara, G. Yáñez, Relación entre el espesor elástico de la litosfera y la segmentación tectonica del margen andino (15–47°), Rev. Geol. Chile 30 (2) (2003) 159–186.

[55] A. Tassara, Interaction between the Nazca and South American plates and formation of the Altiplano–Puna plateau: review of a flexural analysis along the Andean margin (15°–34°s), Tectonophysics 399 (2005) 39–57.

[56] M.K. McNutt, Influence of plate subduction on isostatic compensation in northern California, Tectonics 2 (4) (1983) 399–415.

[57] G. Ojeda, D. Whitman, Effect of windowing on lithosphere elastic thickness estimates obtained via the coherence method: results from northern South America, J. Geophys. Res. 107 (B11) (2002) 2275, doi:10.1029/2000JB000114.

[58] J. Nunn, J. Aires, Gravity anomalies and flexure of the lithosphere at the Middle Amazon Basin, Brazil, J. Geophys. Res. 93 (B1) (1988) 415–428.

[59] M.I. Jácome, N. Kusznir, F. Audemard, S. Flint, Formation of the Maturín Foreland Basin, eastern Venezuela: thrust sheet loading or subduction dynamic topography, Tectonics 22 (5) (2003) 1046, doi:10.1029/2002TC001381.

[60] B. Parsons, J. Sclater, An analysis of the variation of ocean floor bathymetry and heat flow with age, J. Geophys. Res. 82 (B5) (1977) 802–827.

[61] C.A. Stein, S. Stein, A model for the global variation in oceanic depth and heat flow with lithospheric age, Nature 359 (1992) 123–129.

[62] C. Schobbenhaus, A. Bellizzia, Geological map of South America, scale 1:5 000 000, CGMW–CPRM–DNPM–UNESCO, Brasilia, Brazil, 2001.

[63] C.R. Ranero, J. Phipps Morgan, K. McIntosh, C. Reichert, Bending-related faulting and mantle serpentinization at the Middle America trench, Nature 425 (2003) 367–373.

[64] E. Daly, C.D. Brown, C.P. Stark, C.J. Ebinger, Wavelet and multitaper coherence methods for assessing the elastic thickness of the Irish Atlantic margin, Geophys. J. Int. 159 (2) (2004) 445–459.

[65] Y. Zhou, G. Nolet, F.A. Dahlen, G. Laske, Global upper-mantle structure from finite-frequency surface-wave tomography, J. Geophys. Res. 111 (2003) B04304, doi:10.1029/2005JB003677.

[66] I. Jackson, Progress in the experimental study of seismic wave attenuation, Annu. Rev. Earth Planet. Sci. 21 (1993) 375–406.

[67] R. Montelli, G. Nolet, A. Dahlen, G. Masters, R. Engdahl, S.-H. Hung, Finite-frequency tomography reveals a variety of plumes in the mantle, Science 303 (2004) 338–343.

[68] S. Cloetingh, P. Ziegler, F. Beekman, P. Andriessen, L. Matenco, G. Bada, D. Garcia-Castellanos, N. Hardebol, P. Dézes, D. Sokoutis, Lithospheric memory, state of stress and rheology: neotectonic controls on Europe's intraplate continental topography, Quat. Sci. Rev. 24 (3–4) (2005) 241–304.

[69] A. Maggi, J.A. Jackson, D. McKenzie, K. Priestley, Earthquake focal depths, effective elastic thickness and the strength of the continental lithosphere, Geology 28 (6) (2000) 495–498.

[70] J. Jackson, Strength of the continental lithosphere: time to abandon the jelly sandwich? GSA Today 12 (9) (2002) 4–10.

[71] A.B. Watts, E.B. Burov, Lithospheric strength and its relationship to the elastic and seismogenic layer thickness, Earth Planet. Sci. Lett. 213 (2003) 113–131.

[72] M.R. Handy, J.-P. Brun, Seismicity, structure and strength of the continental lithosphere, Earth Planet. Sci. Lett. 223 (2004) 427–441.

[73] E.R. Engdahl, R.D. van der Hilst, R. Buland, Global teleseismic earthquake relocation with improved travel times and procedures for depth determination, Bull. Seismol. Soc. Am. 88 (1998) 722–743.

[74] H. Lyon-Caen, P. Molnar, G. Suarez, Gravity anomalies and flexure of the Brazilian Shield beneath the Bolivian Andes, Earth Planet. Sci. Lett. 75 (1) (1985) 81–92.

[75] A.B. Watts, S. Lamb, J.D. Fairhead, J.F. Dewey, Lithospheric flexure and bending of the Central Andes, Earth Planet. Sci. Lett. 134 (1995) 9–21.

[76] X. Yuan, S.V. Sobolev, R. Kind, O. Oncken, G. Bock, G. Asch, B. Schurr, F. Graeber, A. Rudloff, W. Hanka, K. Wylegalla, R. Tibi, C. Haberland, A. Rietbrock, P. Giese, P. Wigger, P. Röwer, G. Zandt, S. Beck, T. Wallace, M. Pardo, D. Comte, Subduction and collision processes in the Central Andes constrained by converted seismic phases, Nature 408 (2000) 958–961.

[77] ANCORP Working Group, Seismic imaging of a convergent continental margin and plateau in the Central Andes (Andean Continental Research Project 1996 (ANCORP'96)), J. Geophys. Res. 108 (B7) (2003) 2328, doi:10.1029/2002JB001771.

[78] S. Lamb, Vertical axis rotation in the Bolivian orocline, South America 1. Paleomagnetic analysis of Cretaceous and Cenozoic rocks, J. Geophys. Res. 106 (B11) (2001) 26,605–26,623.

[79] D. Hindle, J. Kley, O. Oncken, S.V. Sobolev, Crustal balance and crustal flux from shortening estimates in the Central Andes, Earth Planet. Sci. Lett. 230 (2005) 113–124.